The Astrophysical Journal, 897:92 (15pp), 2020 July 1 https://doi.org/10.3847/1538-4357/ab9a41

Large-format X-Ray Reflection Grating Operated in an Echelle-like Mounting

Casey T. DeRoo[1], Randall L. McEntaffer[2], Benjamin D. Donovan[2], Fabien Grisé[2], Chad Eichfeld[3], Vadim Burwitz[4], Gisela Hartner[4], Carlo Pelliciari[4], and Marlis-Madeleine La Caria[4]
[1] The University of Iowa, Dept. of Physics & Astronomy, Van Allen Hall, Iowa City, IA 52242, USA; casey-deroo@uiowa.edu
[2] The Pennsylvania State University, Dept. of Astronomy & Astrophysics, 505 Davey Lab, University Park, PA 16802, USA
[3] The Pennsylvania State University, Materials Research Institute, N-153 Millennium Science Complex, University Park, PA 16802, USA
[4] Max-Planck Institute for Extraterrestrial Physics (MPE), Giessenbachstr. D-85748, Garching, Germany
Received 2020 February 21; revised 2020 June 4; accepted 2020 June 5; published 2020 July 7

Abstract

We report on resolving power measurements of an X-ray reflection grating designed for use in an astronomical soft X-ray spectrograph. The grating was patterned via electron-beam lithography (EBL) to have fanned grooves to match the convergence of an illuminating beam. Grating measurements were conducted in an echelle-like mounting, which yields access to high diffraction orders in the soft X-ray bandpass (0.2–2.0 keV). By comparing the zeroth-order line-spread function to the telescope focus, we find evidence for minimal broadening ($<1''$) introduced by the figure of the grating. In addition, we fit for the spectral resolution ($R = \lambda/\Delta\lambda$) intrinsic to this grating using a Bayesian Markov Chain Monte Carlo approach. Using an ensemble fitting technique, we find that the grating resolution R exceeds 2200 (3σ lower bound). This current grating resolution meets the performance required for a notional soft X-ray grating spectroscopy mission measuring hot baryonic material in the extended halos of galaxies. Using ray-trace simulations, we identify a geometric aberration resulting from path length differences across the width of the grating as a limiting factor in assessing the resolution of these gratings and discuss methods for placing better constraints on the inherent resolution of X-ray astronomical reflection gratings fabricated using EBL.

Unified Astronomy Thesaurus concepts: Astronomical instrumentation (799); Spectroscopy (1558); Astronomical techniques (1684); Bayesian statistics (1900)

1. Introduction

In the soft X-ray band (0.2–2.0 keV), gratings are employed to form dispersive astronomical instruments for spectroscopy. Several rocket-borne spectrometers (e.g., WRX, Miles et al. 2019; EXOS, Oakley et al. 2013) utilize reflection gratings to form low-resolution spectra of diffuse objects bright in the soft X-ray. Within observatory-class instruments, both the Reflection Grating Spectrometer aboard XMM-Newton (RGS; den Herder et al. 2001) and the transmission grating spectrometers aboard the Chandra X-ray Observatory (HETG, Canizares et al. 2005; LETG, Brinkman et al. 2000) have been in productive operation for roughly two decades. Future proposed X-ray missions, such as Lynx (Gaskin et al. 2019) and Arcus (Smith et al. 2019), are baseline grating spectrometers with order-of-magnitude improvements in effective area (EA) and line detection sensitivity over existing X-ray grating spectrometers.

The performance requirements for the Arcus and Lynx spectrometers are influenced by the EA and spectral resolution R ($\lambda/\Delta\lambda$) needed to resolve absorption lines produced by baryonic material distributed in the hot extended halos of galaxies and clusters. Detections of the Sunyaev–Zel'dovich effect in stacked galaxy measurements (de Graaff et al. 2019; Tanimura et al. 2019) provide evidence of significant baryonic mass out to and beyond the virial radius. UV absorption-line studies (e.g., Lehner et al. 2007; Danforth & Shull 2008) have placed constraints on the mass content (20%–40%) of the "warm" phase ($\lesssim 10^{5.5}$ K) of this material. However, the "hot" phase ($\gtrsim 10^{6}$ K) is thought to contain more of these gaseous baryons, accounting for as much as 50% of the total and 90% of metals (Cen & Ostriker 2006; Shull et al. 2012). At the temperatures of the "hot" phase, astrophysically abundant metals contribute to the X-ray spectrum predominantly through bound–bound lines (Bregman 2007). Bregman et al. (2015, hereafter B15) assess prominent lines produced by ions present in 10^{6}–$10^{8.2}$ K gas and find that O VII Heα (574 eV) and O VIII Lyα (654 eV), both in the soft X-ray bandpass, are promising lines for detecting baryonic material in this hot phase.

To that end, Kovács et al. (2019) report the detection of the O VII Heα line in the Chandra LETG spectrum of H1821+643. However, they detect the presence of this line without resolving the individual absorption-line structures in the X-ray spectrum. Their method relies on previously measured UV absorption-line systems at known z and stacking redshifted X-ray spectra along a well-observed (470 ks) sight line to generate a 3.3σ detection of an O VII absorption feature. This detection lends credence to using X-ray absorption-line spectroscopy to detect and characterize these unaccounted-for hot baryons, while also demonstrating the limitations of using current instrumentation. B15 compute the required performance for a grating spectroscopy mission capable of independently detecting a statistically significant number of absorption systems in promising active galactic nucleus sight lines. They find that such an instrument must have a minimum resolution of $R > 2000$ and an EA of at least 300 cm^2 at 0.5 keV.

1.1. Conical Reflection Grating Geometry

Achieving this EA over a broad bandpass demands a grazing incidence optical system, since reflections at angles above the critical angle rapidly reduce throughput. As such, multiple X-ray reflection gratings must be tightly packed in modules to yield a spectrometer with the required EA. However, this stacking prohibits working at high diffraction orders if the grooves are perpendicular to the incoming beam and diffraction happens in the plane of incidence, as done for XMM-Newton's

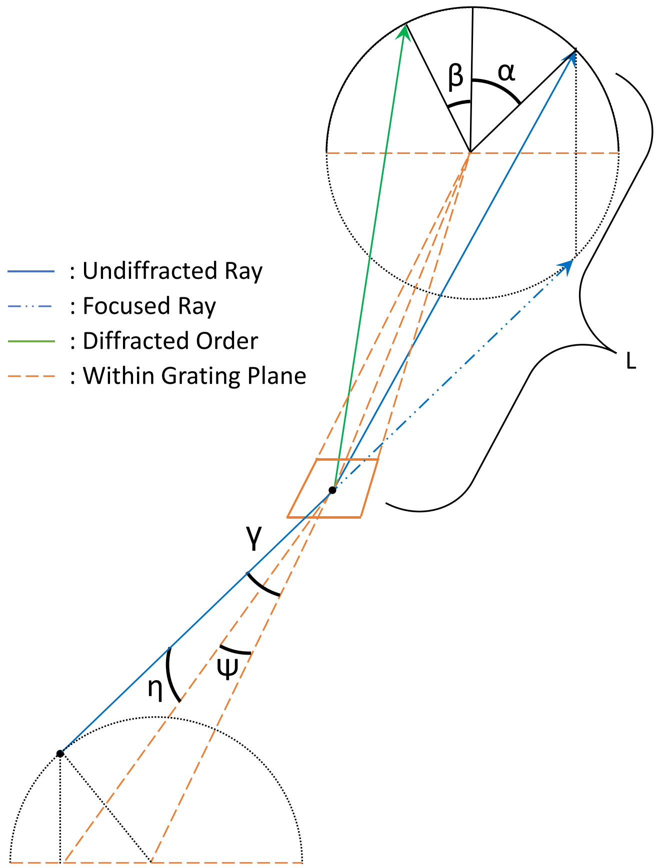

Figure 1. Diagram of the generalized conical diffraction geometry.

RGS. High diffraction orders from one grating are vignetted by the grating stacked above. Restricting spectroscopy to low orders in turn places a limitation on the spectral resolution achievable with this in-plane dispersive optical system.

However, a grazing incidence echelle spectrograph (Cash 1982) can enable operation at high orders without a significant loss of throughput. This conical diffraction geometry has been previously described elsewhere (e.g., Cash 1982; McEntaffer et al. 2013; McEntaffer 2019). An echelle-like mounting with a shallow cone angle yields a diffraction pattern in a plane perpendicular to the groove direction, following the generalized grating equation (Equation (1)):

$$\sin\alpha + \sin\beta = \frac{n\lambda}{d\,\sin\gamma}, \tag{1}$$

where d is the groove period, λ is the wavelength of the incident light, n is the diffracted order number, α is the angle between zeroth-order reflection and the grating normal as projected on the focal plane, β is the angle of the diffracted order and the grating normal, and γ is the cone angle formed between the central groove direction and the incident ray. This geometry is shown in Figure 1. Pursuant to Figure 1, we define the additional variables η, the grazing incidence angle between the grating plane and the incident light, Ψ, the angle between the central groove and the incident light as projected into the grating plane, and L, the distance between the center of the grating and the zeroth-order spot. This diffraction pattern leaves orders with high angular dispersion accessible at the same focal plane as the undiffracted beam and does not vignette high orders in astronomical applications requiring nested gratings. Furthermore, by employing a blazed grating, the grazing incidence equivalent of the Littrow configuration can be realized, yielding efficient high-order operation (Miles et al. 2018).

In order to realize high spectral resolution in this conical mounting, however, the groove pattern must be radially ruled. A grating for which the grooves converge at the center of the diffraction circle, called the grating groove hub, diffracts and preserves the focus of a converging beam of light. This groove pattern must match the angular convergence of the imaging system toward the focal plane. Manufacturing a grating with this groove pattern poses a challenge for techniques such as mechanical ruling and photolithography, since the relative angular change between adjacent grooves is vanishingly small.

In the present work, we describe the characterization and test of a large-format (100 mm × 70 mm) X-ray reflection grating designed for operation in a conical mounting. This grating was patterned using electron-beam lithography (EBL), a flexible lithography technique in which a beam of high-energy electrons is rastered over resist to produce a pattern. EBL routinely achieves feature sizes on the order of tens of nanometers, and isolated features with critical dimensions on the order of a few nanometers have been previously demonstrated (e.g., Manfrinato et al. 2013). Moreover, the patterns produced are highly customizable, making EBL suitable for producing this radially ruled groove pattern. By operating this grating in conjunction with a silicon pore optics telescope (SPO; Collon et al. 2019 and references therein) at the PANTER X-ray Test Facility, we realize an echelle-like grazing incidence spectrometer system and measure diffracted orders at echelle angles of 35°–64°. We assess the line-spread functions (LSFs) produced by this grazing incidence system and estimate the resolving power of the large-format grating by performing an ensemble fit to the diffracted LSFs.

2. Methods

2.1. Test Facility and Optical Components

X-ray measurements were conducted at the PANTER X-ray Test Facility (Burwitz et al. 2019), an X-ray beamline specializing in the testing and characterization of X-ray astronomical systems (e.g., Predehl et al. 2016; Saha et al. 2018; Bradshaw et al. 2019). X-ray sources are housed at one end of a 122 m, 1 m diameter beamline and used to illuminate optics in a 12 m long, 3.5 m diameter instrument chamber at the opposite end. X-ray systems under test can be mounted to an adaptable optical bench and aligned in situ using vacuum-compatible remote staging. *TRoPIC*, an X-ray CCD with subpixel reconstruction good to 40 μm (Meidinger et al. 2009), was placed on vacuum-compatible remote staging at the nominal focal plane of the X-ray optical system. The measurements described herein use this detector exclusively.

The reflection grating was tested in conjunction with an SPO telescope (Collon et al. 2019). SPO are an X-ray telescope technology formed by stacking wedged silicon plates on a mandrel with a given optical prescription to form an SPO stack (Keek et al. 2019). Primary and secondary SPO stacks are then aligned and mounted in brackets to form an X-ray optical unit (XOU), which is a two-reflection, grazing incidence telescope (Barriére et al. 2019; Landgraf et al. 2019; Vacanti et al. 2019).

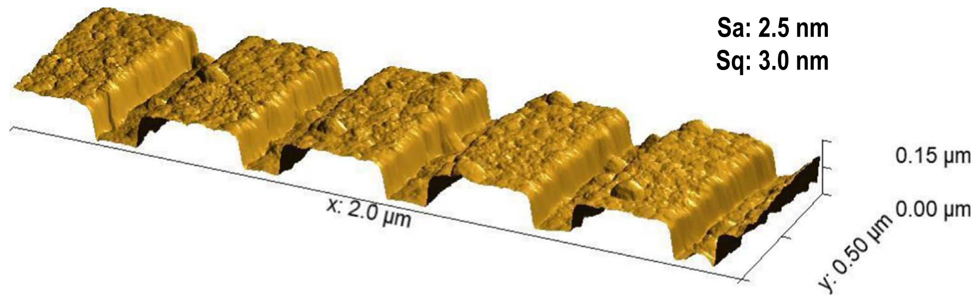

Figure 2. Atomic force micrograph of the fabricated reflection grating. This micrograph covers a 2.0 μm by 0.5 μm area near the center of the grating. Measurements of the arithmetical mean height Sa and rms height Sq on the upper surface of the grating yield values of 2.5 and 3.0 nm, respectively.

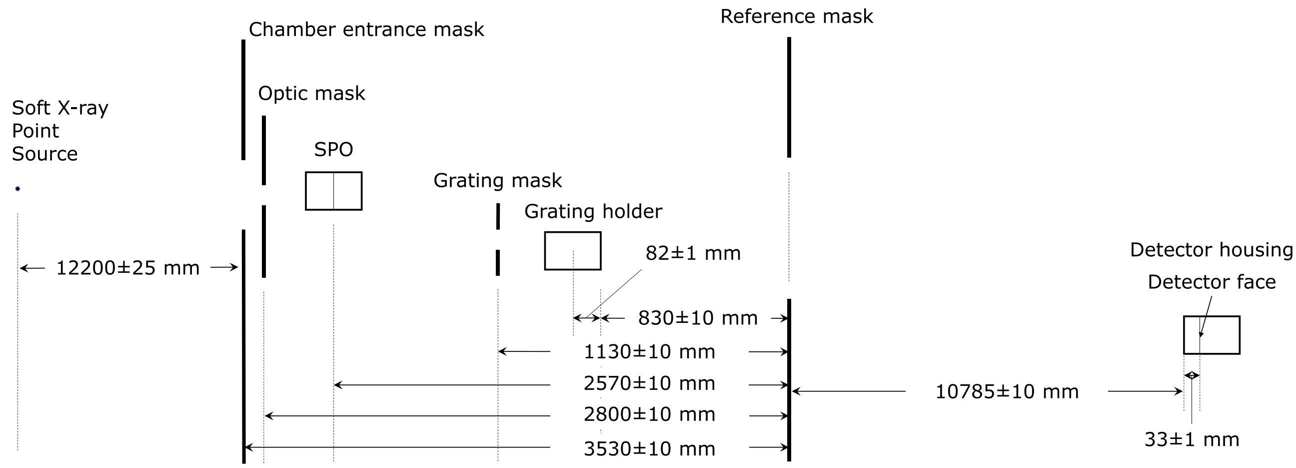

Figure 3. Cartoon showing the optical setup for the grazing incidence grating spectrometer system under test. Distances are not to scale. Measurements are along the optical axis and are given with the CCD in the position of the SPO focus. Errors are estimated based on the repeatability of separate laser-distance meter measurements or based on machine tolerances.

An XOU forms the base unit of SPO, and the modular design of SPO permits many XOUs to be aligned into a larger telescope assembly, as is planned for the European Space Agency's ATHENA mission (Bavdaz et al. 2019). The optical prescription for an SPO XOU is defined by its focal length z_0 and the radius of curvature of its central plate r_0. The SPO employed for these X-ray measurements is XOU0038, manufactured for the Arcus Medium-class Explorer (MIDEX) mission concept by cosine Research BV. The XOU has a focal length of $z_0 \sim 12.0$ m and a radius of curvature of 737.0 mm, resulting in a graze angle of approximately $i = 0\overset{\circ}{.}88$.

The reflection grating was fabricated at the Pennsylvania State University's Materials Research Institute. A 6-inch-diameter, 1.5 mm thick silicon wafer was employed as the grating substrate. This wafer was then coated with resist and patterned using a Raith EBPG5200 EBL tool. The grating patterning process via EBL is described in greater detail by Miles et al. (2018). The grating pattern is designed to have a 400 nm period at the center of the grating and is fanned so as to converge to a point 11,749.41 mm away from the center of the grating. The grating pattern measures 100 mm in the dispersion direction (orthogonal to the grooves) and 70 mm in the axial direction (along the grooves). Following the EBL write, the resist was developed and transferred to the underlying silicon substrate via an anisotropic reactive-ion etch, leaving a laminar groove pattern. An atomic force micrograph of the grating pattern produced is shown in Figure 2.

2.2. Optical System Alignment

Ideally, the spectrometer system is aligned such that the SPO radial direction, the cross-dispersion direction of the gratings, and the horizontal axis of the CCD are all parallel. This minimizes the size of the point-spread function (PSF) in the dispersion direction of the grating, since the PSF of an azimuthal segment of an X-ray telescope is highly asymmetric (see Section 3.2). Achieving this alignment increases the experiment's sensitivity to measuring the inherent spectral resolution of the grating.

A cartoon of the optical path of the experiment is shown in Figure 3. The grazing incidence spectrometer system is illuminated by a point-like soft X-ray source located 122 m away from the chamber entrance and hence is a spherical wave front with mild (but nonnegligible) curvature. This wave front passes through the chamber entrance mask and an optics mask sized to the SPO XOU dimensions. This serves to fully illuminate the SPO XOU while minimizing X-ray stray light. The finite distance of the source displaces the position of the telescope's best focus to 13.39 m away from the optic, resulting in a plate scale of 64.89 μm per arcsecond.

Aligning the SPO and grating to form a grazing incidence spectrometer system proceeds sequentially along the photon path. The radial and azimuthal directions of the SPO are first aligned relative to the CCD horizontal and vertical directions, respectively. This places the SPO in the "parentheses" configuration relative to gravity. Alignment begins by imaging the direct beam through the SPO without a reflection. This produces an array of pore images with shadows created by the

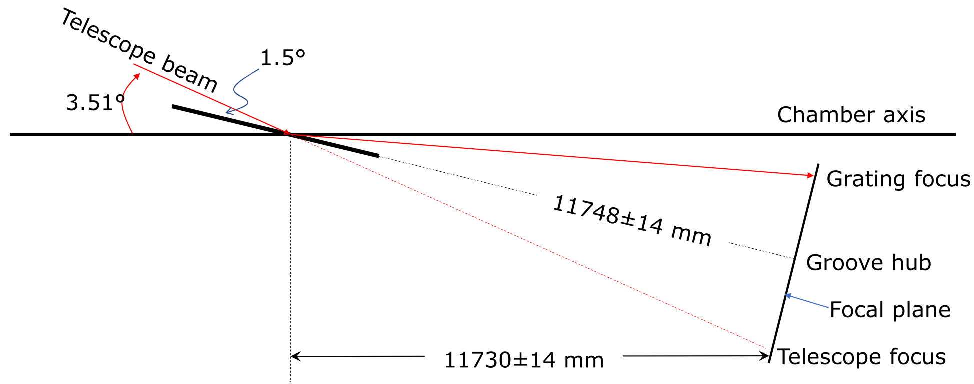

Figure 4. View of the grating along the dispersion axis following positional alignment. Both reported distances are calculated based on measurements reported in Figure 3. All distances are given in mm.

pore walls and wafer surfaces on the detector. The SPO is then pitched (i.e., rotated about the gravity vector) and the light produced by a single reflection within the SPO traced across the fixed CCD. This determines the radial direction of the SPO module relative to the horizontal axis of the CCD. As both the radial/azimuthal directions of the SPO and the horizontal/vertical directions of the CCD are orthogonal by definition, the SPO is aligned to the fixed CCD axes.

The next step is to establish the orientation of the stage stacks that translate the CCD relative to these axes. While looking at the array of pore images through the SPO without reflection, the center of the SPO stack is determined as a horizontal position on the CCD. The SPO is then placed at its nominal pitch angle to form a double-reflection image at the focal plane. The horizontal stage is then moved to the focus and the position on the CCD is then compared to the center of the SPO stack determined via the straight-through image. This determines the horizontal stage attitude relative to the radial direction. Finally, while at the SPO focus, the vertical detector stage is then translated across the focus image to measure the orthogonality of the vertical stage relative to the horizontal stage. A drift in CCD Y of the static focus demonstrates nonorthogonality of these two stages. After the completion of this step, the optic radial and azimuthal directions, the CCD horizontal and vertical axes, and the horizontal stage attitude are known relative to one another, and the orthogonality of the detector stages is also known. After obtaining the prime focus of the SPO through pitch, yaw, and focus scans, the optic is fixed.

Next, the position of the machined grating mask is adjusted. The grating mask has an aperture stop for the telescope beam, minimizing the illumination of unruled grating area. Unruled areas are prone to high roughness and curvature. Vignetting these unruled areas is necessary to accurately assess the zeroth-order LSF and hence constrain the spectral resolution of the grating. The relationship between the position of the grating mask and the optical system was mapped out in two ways. First, the grating mask was illuminated using the straight-through telescope beam. The mask shadows were used to position the mask such that the vertical bisector of the slits is coincident with the radial direction of the SPO. This exercise also provides an initial estimate for positioning the slit radially in the focused telescope beam. This radial position was fine-tuned by translating the slit mask across the focused telescope beam and recording the flux in the optic focus. As the slit mask travels across the telescope beam, the measured intensity in the SPO focus varies smoothly from zero when occulted to full intensity when passing through the slit.

Following placement of the mask, the grating is translated to establish its placement relative to the telescope beam. The horizontal and vertical placement of the grating is achieved by mapping the shadow of the grating position in the straight-through beam of the SPO. The center of the grating in the vertical direction is aligned to the SPO by placing the bisector of the grating width along the bisector of the SPO in azimuth. The intended offset in the radial direction is known and the grating is placed horizontally according to this distance. The remaining linear alignment, distance along the optical axis, arises from the need to place the converging grooves of the radial pattern at the appropriate distance from the focal plane. The grating was installed in the chamber near this nominal position, and a laser-distance meter was used to determine distances as reported in Figure 3. These measurements were then used to compute the translation needed to bring the grating into position along the optical axis and hence set the distance between the center of the grating and the focal plane (Figure 4).

Next, the grating pitch and roll axes are aligned. This begins by placing the grating in the SPO beam at the nominal test pitch and imaging the zeroth-order reflection. The pitch is decreased until the reflected spot returns to the SPO focus spot, thus defining the grating stage position at which zero pitch is achieved. To align the grating in roll, a series of images of the zeroth-order reflection is created as the pitch is increased to $1\overset{\circ}{.}5$, the nominal graze angle for testing. If the roll of the grating is not aligned to the horizontal stage axis, the centroid of the zeroth-order reflection will drift in azimuthal direction of the SPO during this series. The roll orientation of the grating is then adjusted until the centroids of this series of zeroth-order images lie along the line defining the SPO radial direction with respect to the horizontal stage axis. Following these steps, grating pitch and roll are calibrated, and the cross-dispersion and dispersion axes of the grating are aligned with the SPO radial and azimuthal directions, respectively.

To complete the process of aligning the grating, the yaw of the grating is determined. At the nominal pitch of $1\overset{\circ}{.}5$, $\pm$1st orders are found at the focal plane. If the grating yaw $\Psi = 0°$, the centroid of these orders is at the same cross-dispersion position, and the line connecting them is parallel to the dispersion direction of the grating. By performing a series of shallow exposures, the grating yaw is adjusted until this condition is reached. In this investigation, the yaw alignment was further refined by repeating this process at $\pm$3rd order.

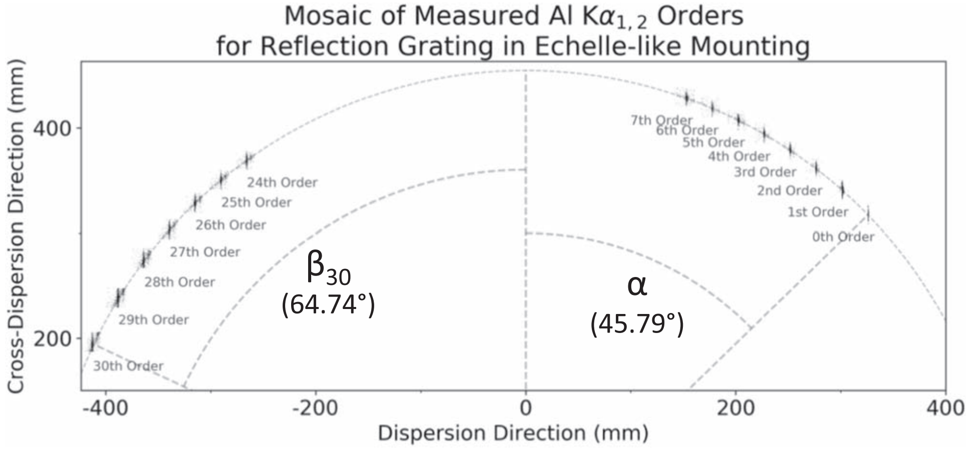

Figure 5. Mosaic image of the diffraction pattern produced by the X-ray reflection grating in the echelle-like mounting. The stage positions of each measurement along with the line centroids were used to reconstruct the mosaic and the prescription of the diffraction arc. With reference to Equation (1), labels for α, β_{30} have been added.

Lastly, the relative position of the grating and grating mask is verified. We employ a 1.31 mm wide slit in the grating mask, which equates to illuminating ∼50 mm along the grating groove direction. By translating the grating horizontally across the telescope beam, the flux in the optic focus varies. This flux mapping shows structure that indicates the shadow of the grating substrate. In addition, this flux mapping is used as a secondary verification on pitch alignment. Since small errors ($\sim 0^{\circ}.1$) in pitch increase the projected thickness of the grating, the size of the grating shadow can be measured by this flux mapping and used as a secondary correction on the pitch angle of the grating. Following these steps, the grating is centered on the 1.31 mm slit in the grating mask and the alignment process complete.

To measure diffracted orders at high dispersions, the grating was placed into an echelle-like configuration by rotating the grating about its surface normal by an angle Ψ. Yawing the grating in this manner increases the cone angle γ without changing the graze angle η. Since

$$\frac{\sin\eta}{\sin\gamma} = \cos\alpha, \tag{2}$$

this increases α, permitting solutions of the grating equation for higher-order n (Equation (1)).

3. Measurements and Analysis

3.1. Echelle-like Test Geometry

Following this alignment procedure, we next validated our test geometry through X-ray measurements of diffracted orders. Figure 5 displays a mosaic of the diffracted orders of Al K$\alpha_{1,2}$ measured in this test configuration. The centroids of these diffracted orders are calculated, and a least-squares fit of a circle to these points is used to compute parameters for the tested grating configuration. These parameters are reported in Table 1; errors in these parameters are derived by propagating the 1σ uncertainty in the best-fit circle to the diffraction geometry.

The manufactured X-ray grating under test is not a true echelle, since the grating profile is laminar rather than blazed. However, we term this configuration "echelle-like" given this configuration's access to diffracted orders at large diffraction angles. For 24th–30th orders, β_n ranges from 35° to 64° and the centroids are displaced a distance of 550–700 mm from zeroth order.

Table 1
Geometric Parameters for the Configuration under Test

Geometric Parameter	Value (Å)
η	$1^{\circ}.537 \pm 0^{\circ}.002$
γ	$2^{\circ}.220 \pm 0^{\circ}.003$
α	$45^{\circ}.79 \pm 0^{\circ}.08$
Ψ	$1^{\circ}.59 \pm 0^{\circ}.04$

Note. Parameters are given with reference to Figure 1. Errors are 1σ.

Deep exposures of Al Kα zeroth, 27th, 29th, and 30th orders were measured in this test configuration.[5] As the dispersion direction of the grating has been aligned to the horizontal direction of the detector, the spectral information of the LSFs can be obtained by summing the data in the vertical direction, forming a one-dimensional profile. The raw X-ray images and the resulting LSFs are shown in Figure 6. These data form the basis for our analysis of the grating's spectral resolution performance.

3.2. Comparing Zeroth Order to the SPO Focus

To assess the impact of grating figure on the achieved spectral resolution of the spectrometer system, we compared the zeroth-order LSF to the focus of the SPO telescope. Measurements of the SPO telescope focus, the zeroth-order LSF, and the dispersion direction profiles are shown in Figure 7. Qualitatively, we note that features of the SPO focus, such as the asymmetric core and the "wings" of the PSF, are reproduced by the grating, albeit with a reflection as expected. Quantitatively, we computed the width and 1σ errors of the SPO focus to be $\mathrm{FWHM_{SPO}} = 106 \pm 2\ \mu$m and the width of the zeroth-order LSF to be $\mathrm{FWHM}_{n=0} = 121 \pm 5\ \mu$m. Hence, we observe a broadening of the telescope focus from the addition of the reflection grating by $0''.9 \pm 0''.2$.

[5] While 28th order is accessible, efficiency calculations predict that this order is highly inefficient in this mounting configuration. Hence, 28th order was not measured deeply enough to provide a useful constraint on the grating resolution R.

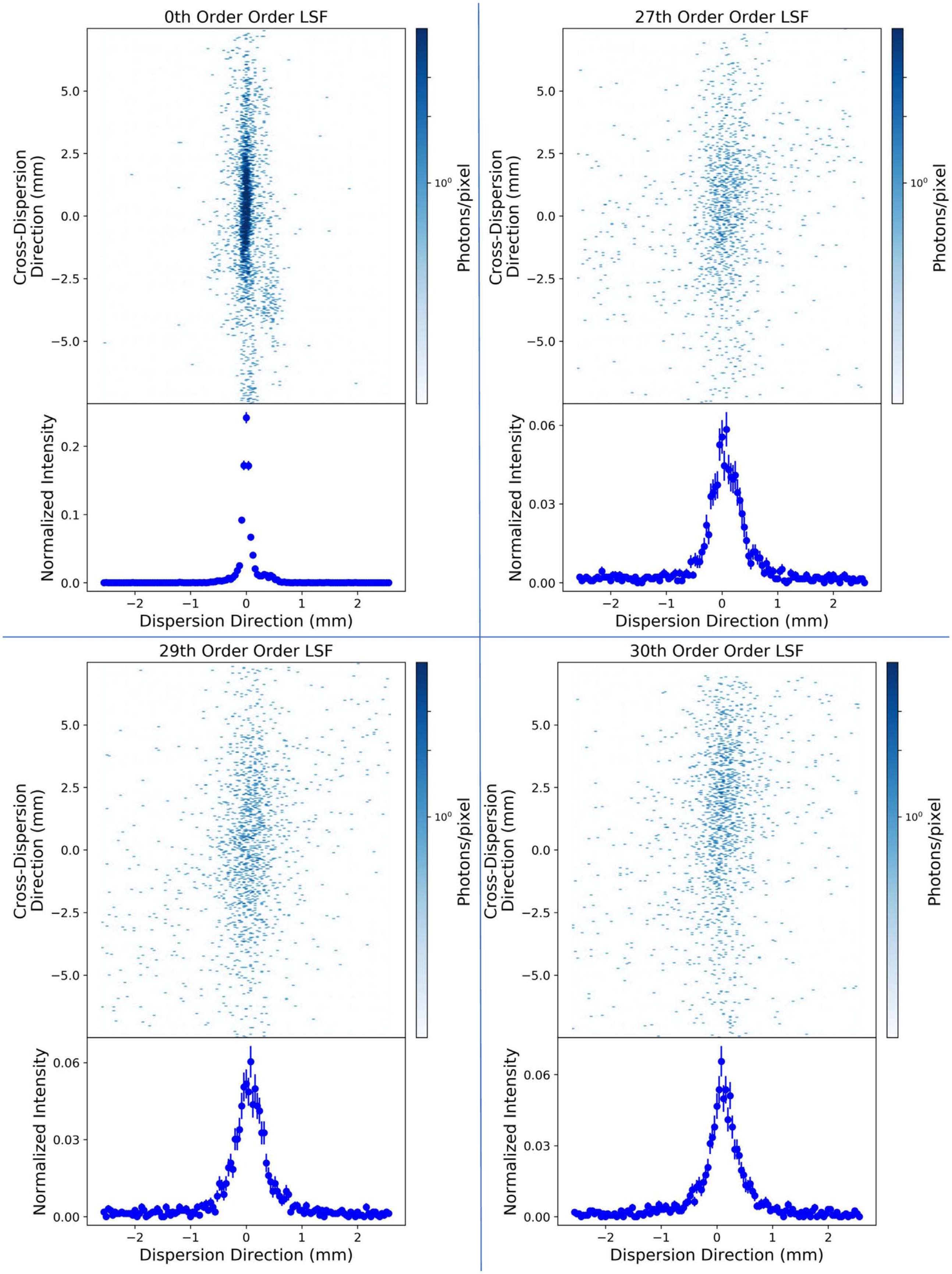

Figure 6. Deep exposures of Al K$\alpha_{1,2}$ zeroth (top left), 27th (top right), 29th (bottom left), and 30th (bottom right) orders. The CCD images have been summed along the vertical direction to form the one-dimensional profile in the dispersion direction along the bottom of each frame. In these images and profiles, wavelength increases with positive x (i.e., the dispersion vector is to the right). Error bars show the Poisson counting error in each bin, and profiles are normalized so as to integrate to unity.

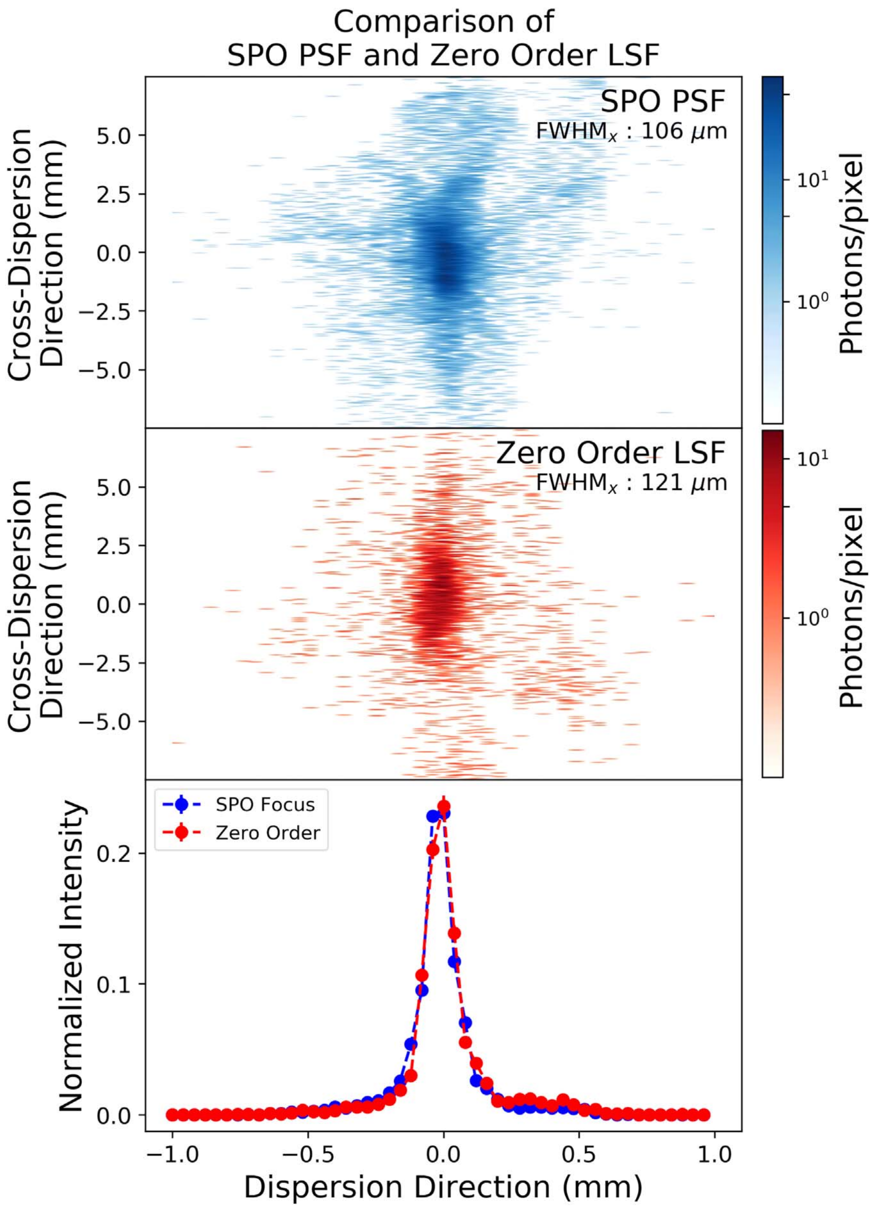

Figure 7. Measurements of the SPO focus (top), the zeroth-order LSF (middle), and the dispersion profiles of each (bottom). Features in the SPO focus are present but vertically flipped, and the dispersion dimension profiles are similar.

As an independent assessment of the grating figure, the X-ray grating was measured using an optical profilometer following mounting but prior to installation in the PANTER test chamber. As limitations on the total travel of the profilometer stage precluded measuring the entire grating, a subsection of the reflection grating measuring 35 mm in the dispersion direction and 70 mm along the optical axis was examined using the profilometer. A surface plot of the resulting data is shown in Figure 8.

From these data, we compute the expected broadening of the zeroth-order LSF of $0\farcs3 \pm 0\farcs1$. This is smaller than the broadening observed under X-ray illumination; however, the area of the grating illuminated during the X-ray test (50 mm along the grooves by 100 mm orthogonal to the grooves) is larger than the area that could be sampled with the profilometer. To estimate the broadening that would be produced by the fully illuminated area, the profilometer data are fit with a two-dimensional, third-order polynomial and the

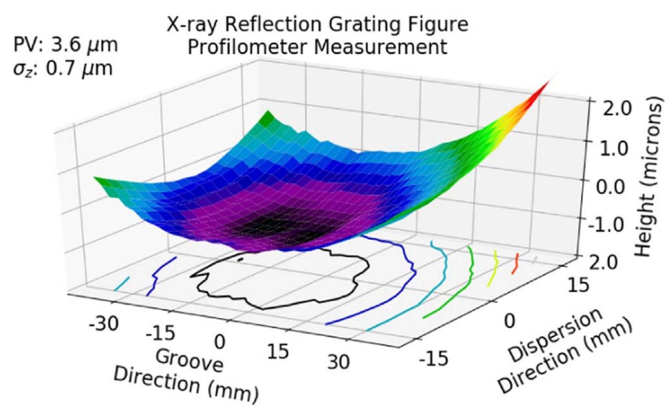

Figure 8. Figure of the interior portion (70 mm $\times$ 35 mm) of the tested grating. Contours separated by 0.5 μm are projected on the Z-axis. The grating figure is dominated by power, typical of Si wafers.

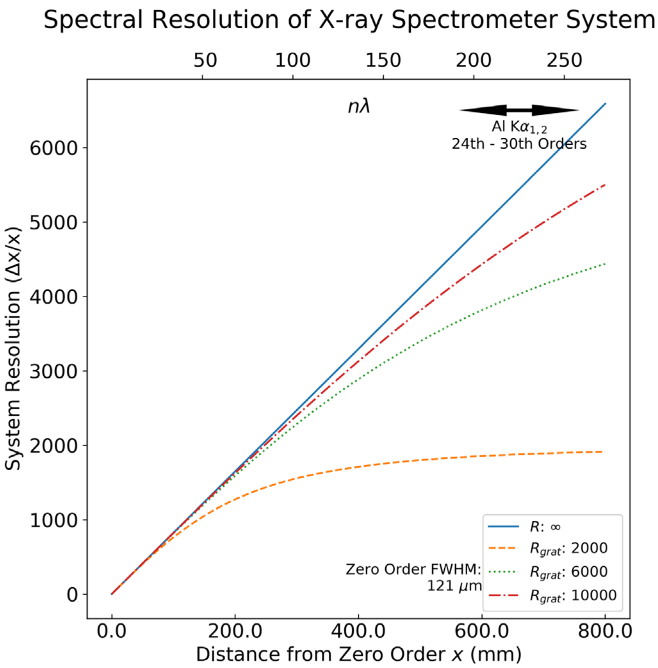

Figure 9. Achieved spectral resolution of the grating spectrometer as a function of dispersed distance. The system resolution is calculated for intrinsic grating resolutions $R = 2000$, 6000, and 10,000. A zeroth-order width of 121 μm is assumed, and the locations of Al K$\alpha_{1,2}$ 24th–30th orders are denoted with a black arrow.

resulting function extrapolated to the size of the illuminated area. Using this extrapolation, the expected broadening is 0$''$9, in keeping with the X-ray measurement. Thus, we posit that the grating figure fully accounts for the observed zeroth-order broadening.

However, slope errors introduced by the grating figure are not the limiting factor in the achieved resolving power of the spectrometer system. The SPO PSF focus quality measures 1$''$6 FWHM in the dispersion direction, and hence the telescope quality is the dominant term in the measured width of the zeroth-order LSF. Figure 9 estimates the system-limited resolution for the spectrometer based on the X-ray measured zeroth-order FWHM. Other grating-induced contributions are quantified using R, and the resulting broadening is added in quadrature to the measured zeroth-order width. We also denote the positions of high diffraction orders of Al K$\alpha_{1,2}$ accessible in the echelle-like mounting. Given the divergence of the resolution curves at these large dispersions, measurements of the 24th–30th diffraction orders permit the assessment of the grating's intrinsic resolution R. We note that beyond $R >$ 10,000, the width of the diffracted LSF is dominated (>90%) by the contribution of the telescope PSF. Hence, R values exceeding this limit are ill constrained by these data.

3.3. Functional Form of the Diffracted LSFs

The LSFs measured in this X-ray test are the responses of the spectrometer to the Al K$\alpha_{1,2}$ fluorescence line complex. A single fluorescence line follows a Lorentzian distribution, with functional form

$$L(\lambda, \lambda_0, \Gamma) = \frac{\Gamma}{\pi[(\lambda - \lambda_0)^2 + \Gamma^2]}, \tag{3}$$

with central wavelength λ_0 and an FWHM of 2Γ. The Al K$\alpha_{1,2}$ doublet consists of two of these closely spaced fluorescence lines, and the spectral source illuminating the grating is modeled as

$$\begin{aligned} \mathrm{AlK}\alpha_{1,2}(\lambda, \lambda_0, \Delta\lambda_0, \Gamma) = & \frac{\Gamma}{\pi[(\lambda - \lambda_0)^2 + \Gamma^2]} \\ & + \frac{\Gamma}{2\pi[(\lambda - (\lambda_0 - \Delta\lambda_0)^2 + \Gamma^2} \end{aligned} \tag{4}$$

where we have parameterized the wavelength separation between these features as $\Delta\lambda_0 = \lambda_0^{\mathrm{K}_{\alpha 1}} - \lambda_0^{\mathrm{K}_{\alpha 2}}$ and assumed the flux ratio $\mathrm{K}\alpha_1/\mathrm{K}\alpha_2 = 2$. Table 2 details the values and errors for the line shape parameters of Al K$\alpha_{1,2}$ adopted in this work.

The LSF measured in response to Al K$\alpha_{1,2}$ illumination depends on the natural line shape (Equation (4)), the spectrometer system focus, and the dispersed grating response. The spectrometer system focus is the zeroth-order LSF, which is the telescope PSF modulo any errors induced by the grating's optical figure. The dispersed grating response consists of errors that broaden the spectral response, such as grating misalignment, geometric limitations, or groove period errors (see Section 4.1). Through the generalized grating equation (Equation (1)), these errors blur the spatial distribution of photons at the focal plane, broadening the LSF and limiting the resolution of the instrument. The LSF response is the convolution of each of these components; hence, we model the observed LSFs using the following expression:

$$\begin{aligned} F(x, n, \theta) = & F(x, n = 0, \theta) \circledast \\ & \times \left\{ \frac{[(G(\lambda, \lambda_0, R) \circledast \mathrm{AlK}\alpha_{1,2}(\lambda, \lambda_0, \Delta\lambda_0, \Gamma)]}{n(\partial\lambda/\partial x)} \right\}. \end{aligned} \tag{5}$$

In Equation (5), $\circledast$ represents the convolution operation, x is the position along the horizontal detector axis in mm, $F(x, n, \theta)$ is the LSF at order n with parameter set θ, $\partial\lambda/\partial x$ is the dispersion relation converting between spectral and spatial coordinates, and $G(\lambda, \lambda_0, R)$ is a normalized Gaussian with FWHM R used to represent any grating-induced broadening.

3.4. Bayesian Modeling of Diffracted LSFs

The measured LSF data are of order 10^3 counts distributed over 50 bins each 40 μm in width. Based on this sparse sampling, the errors are not Gaussian distributed. Moreover, even with substantially deeper measurements than those presented here, the LSF line shape will not fulfill the condition for Gaussian-distributed errors in the LSF wings where the number of counts approaches zero. Thus, χ^2 statistics are inappropriate not only for these sparsely sampled LSF data but even for deep exposures if the data are regularly binned.

To characterize the shape of these LSFs and address this issue of non-Gaussian errors, we use a Bayesian Markov Chain Monte Carlo (MCMC) approach. Bayesian MCMC generates a large number of samples of the posterior probability distribution given a specified prior and likelihood function. This approach probes the range of model parameters θ that describe the measured data D.

Table 2
Literature Values Used for Modeling the Al K$\alpha_{1,2}$ Complex

Al K$\alpha_{1,2}$ Parameter	Value (Å)	Error (Å)	Reference
λ_0	8.33934	$\pm 9.0 \times 10^{-5}$	Bearden & Burr (1967)
$\Delta\lambda_0$	2.244×10^{-3}	$\pm 1.8 \times 10^{-5}$	Heilmann et al. (2019)
2Γ (FWHM)	2.316×10^{-3}	$\pm 4.6 \times 10^{-5}$	Heilmann et al. (2019)

Barring an overall normalization, Bayes's theorem can be written as

$$P(\theta|D) \propto P(D|\theta)P(\theta), \tag{6}$$

where $P(\theta|D)$ is the posterior probability (i.e., probability of the model parameters θ given the observed data D), $P(D|\theta)$ is the likelihood (i.e., probability of the observed data given a model with parameters θ), and $P(\theta)$ is the prior (i.e., the probability of the model parameters θ being accurate given prior information).

The X-ray data are individual photon counts. Hence, the counts in each bin i follow a Poisson distribution with an expected number of counts Λ_i and the associated error $\sigma_i = \sqrt{\Lambda_i}$. The probability of observing N_i counts in a given bin i is thus

$$P(N_i) = e^{-\Lambda_i}\frac{\Lambda_i^{N_i}}{(N_i)!}. \tag{7}$$

An LSF model with a parameter set θ predicts an expected number of counts in each bin $\Lambda_i(\theta)$. The likelihood of measuring data N_0 ... N_T given this model is simply the product of the probabilities given by Equation (7) over T total bins. This makes the log likelihood of observing these data given the model parameterized by θ

$$\log P(D|\theta) = \sum_{i=0}^{T} - \Lambda_i(\theta) + N_i \log\Lambda_i(\theta), \tag{8}$$

modulo a constant that depends only on the observed data N_i and not the model parameters θ. This formulation of the likelihood of observing Poissonian counts over multiple bins is commonly employed for high-energy astronomical observations (Cash 1979).

To sample the posterior distribution $P(\theta|D)$, we adopt Equation (8) as the likelihood function $P(D|\theta)$. To construct the prior $P(\theta)$, we employ uniform distributions that are centered around the parameters' best-known value and bounded by 1σ errors on either side. For parameters related to the K$\alpha_{1,2}$ line complex, center values and bounds are adopted from literature values (see Table 2). The dispersion $\partial\lambda/\partial x$, which sets the relationship between wavelength and the dispersion position, is calculated by taking the change in $n\lambda$ for 27th, 29th, and 30th orders and dividing it by the difference between the order centroids in the dispersion direction. This approach yields values for $\partial \lambda/\partial x(n = 1)$ that fall in the range 0.340750 ± 0.000077 Å mm^{-1}. R is parameterized logarithmically, and its prior is permitted in the range $3 < \log R < 4$. Parameters specific to this set of LSF measurements in this particular optical configuration, such as the overall amplitude of the measured LSF or the absolute position of the LSF centroid, are nuisance parameters for the purpose of constraining R. For these, flat "uninformative" priors with reasonable boundaries are employed; this is equivalent to providing these as bounds for a least-squares fitting routine.

We have utilized *emcee*[6] to perform the MCMC sampling of the posterior probability distribution (Foreman-Mackey et al. 2013). *emcee* is a Python implementation of an Affine Invariant MCMC Ensemble sampler (Goodman & Weare 2010), which is insensitive to the covariance between model parameters. Hence, this method is well suited to sampling distributions with highly correlated parameters such as the distribution at hand, where, for example, the grating resolution R is correlated with parameters describing the zeroth-order line width. The models and likelihood functions described here are constructed in *lmfit*,[7] a Python-based curve-fitting package (Newville et al. 2019) containing a wrapper for *emcee*.

For all MCMC samplings of the posterior distribution, 300 "walkers" W were employed. These walkers function as separate chains exploring a distinct location in parameter space but draw information from all the other walkers to inform subsequent samplings of the posterior distribution. All walkers are initialized around best-fit model parameters found through Nelder–Mead (Nelder & Mead 1965) minimization of the negative log likelihood function, and given a small ($\sim$1%) perturbation to provide an initial sample of the space of the posterior probability. Each walker uses a number of samples $S_{\mathrm{walker}} = 25{,}000$ with a burn-in period of $S_{\mathrm{burn}} = 5000$. S_{walker} and S_{burn} are selected based on tools for estimating the autocorrelation time, which suggest an autocorrelation time of <500 steps for all parameters. The total chain length (WS_{walker}) is thinned by this maximum autocorrelation time of 500 steps, yielding a total of 12,000 independent samples of the posterior probability distribution. For comparison, the Raftery–Lewis diagnostic (Raftery & Lewis 1992) indicates that, for fitting the measured LSFs with our parameter set (Section 3.3), achieving a 5% accuracy in the 0.135% (3σ lower bound) percentile requires <1000 independent samples. Hence, the number of samples of the posterior distribution is large enough that there is <5% error on the computed 3σ lower bound.

3.5. Zeroth-order Modeling

To estimate R_{grat} from the measured 27th, 29th, and 30th LSFs, we first characterize the zeroth-order LSF by finding an empirical model for $F(x,\, n = 0,\, \theta)$. As the PSF of the SPO XOU contains contributions from multiple pores, we expect a model with multiple-peaked components to best describe the measured LSF. However, it is not known a priori how many components are needed to adequately describe the zeroth-order LSF. Hence, we adopt a heuristic approach, fitting the zeroth-order data with a grid of models each featuring a distinct number of Gaussian or Lorentzian components. We assess the quality of each fit with a merit function in order to select the best zeroth-order model.

Individual Gaussian components j are free to vary in amplitude A_G^j, center position $x_{0,G}^j$, and width σ_G^j, while

[6] https://emcee.readthedocs.io/en/stable/
[7] https://lmfit.github.io/lmfit-py/index.html

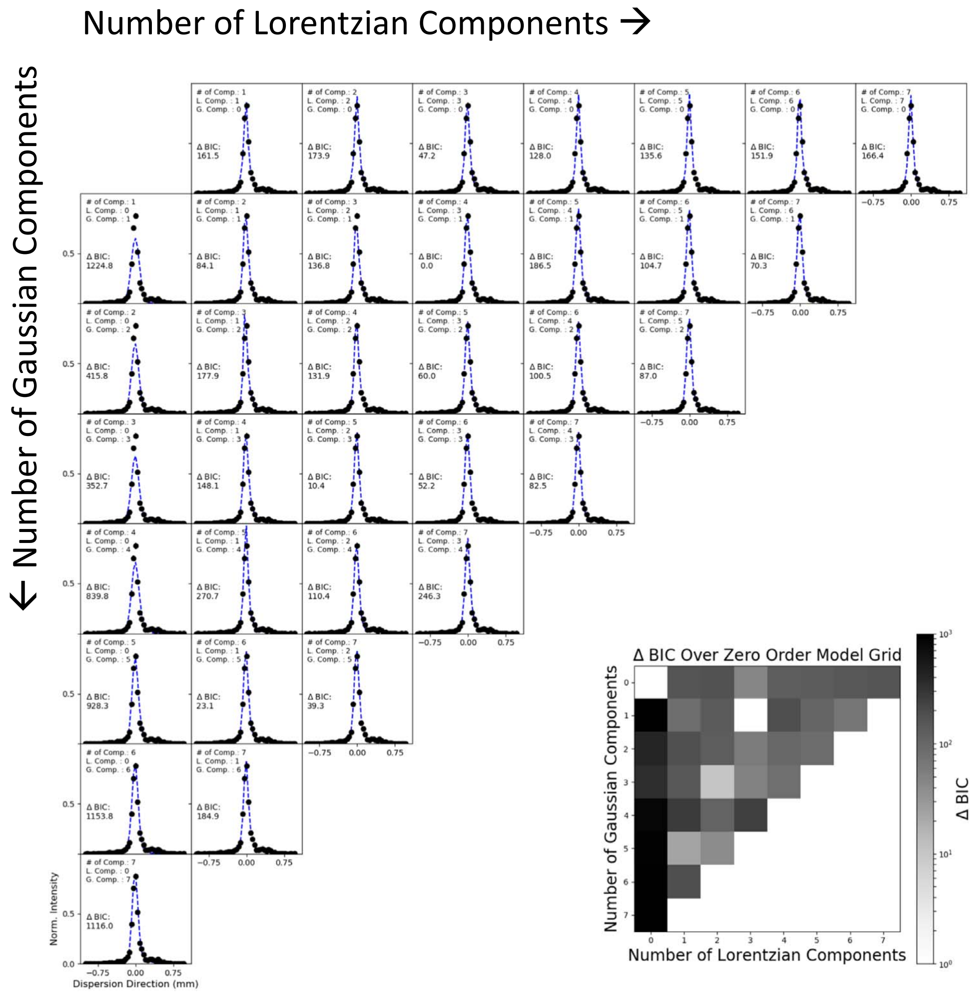

Figure 10. Grid of model fits to the zeroth-order LSF. Models consist of N_C total components, with N_G Gaussian components and $N_C - N_G$ Lorentzian components. Inset text in each of the panels details the number of components in each best-fit model, as well as the change in the BIC merit function. The inset panel at the lower right shows ΔBIC over the model grid.

individual Lorentzian components k have free parameters of amplitude A_L^k, center position $x_{0,L}^k$, and half-width at half-maximum Γ_L^k. The total number of components, N_C, in each zeroth model is $N_C \leqslant 7$, while N_G, the number of Gaussian components, is $0 \leqslant N_G \leqslant N_C$ for each value of N_C. Thus, at each grid position $(N_G, N_C - N_G)$, we fit the model

$$F(x, n = 0, \{\theta\}) = \sum_{j=0}^{N_G} \{G(A_G^j, x_{0,G}^j, \sigma_G^j)\} + \sum_{k=0}^{N_C - N_G} \{L(A_L^k, x_{0,L}^k, \Gamma_L^k)\}, \tag{9}$$

where $\{G(A_G^j, x_{0,G}^j, \sigma_G^j)\}$ is the set of Gaussian components for that grid position, $\{L(A_L^k, x_{0,L}^k, \Gamma_L^k)\}$ is the set of Lorentzian components for that grid position, and the parameter set $\{\theta\}$ contains all relevant free parameters for each component in the zeroth-order model (i.e., $\{\theta\} = \{A_G^j, x_{0,G}^j, \sigma_G^j, A_L^k, x_{0,L}^k, \Gamma_L^k\} \ \forall\ j, k$).

The grid of zeroth-order model fits is shown in Figure 10. To facilitate model selection while avoiding overfitting, we employ the Bayesian information criterion (BIC; Schwarz 1978) as our merit function. The BIC modifies the log likelihood of the fit with a penalty term based on the number of free parameters in the model. To assess the robustness of our zeroth-order model selection, we compute the difference in BIC, ΔBIC, between each other zeroth-order model and the best-fit model. We find that the distribution of this statistic over the explored model space is suggestive of one global minimum (see Figure 10, inset).

Based on this described approach, the zeroth-order best-fit model consists of four components, one Gaussian and three Lorentzian. The best-fit model is shown in Figure 11. We adopt this model, with best-fit parameters $\{\theta\}$, as $F(x, n = 0, \{\theta\})$ in Equation (5) for subsequent fits to the diffracted LSFs.

3.6. Spectral Resolution Analysis via Ensemble LSF Fitting

We fit the diffracted order LSFs as an ensemble to maximize the statistical power of the measured data. To formulate the posterior probability of realizing the ensemble for the MCMC sampler, we employ a formulation of Bayes's theorem that incorporates all three measurements:

$$P(\theta | D_{27\text{th}}, D_{29\text{th}}, D_{30\text{th}}) \propto P(D_{27\text{th}}|\theta) P(D_{29\text{th}}|\theta) P(D_{30\text{th}}|\theta) P(\theta), \tag{10}$$

where $D_{27\text{th}}$, $D_{29\text{th}}$, $D_{30\text{th}}$ are the 27th-, 29th-, and 30th-order data, respectively. In other words, the posterior probability is

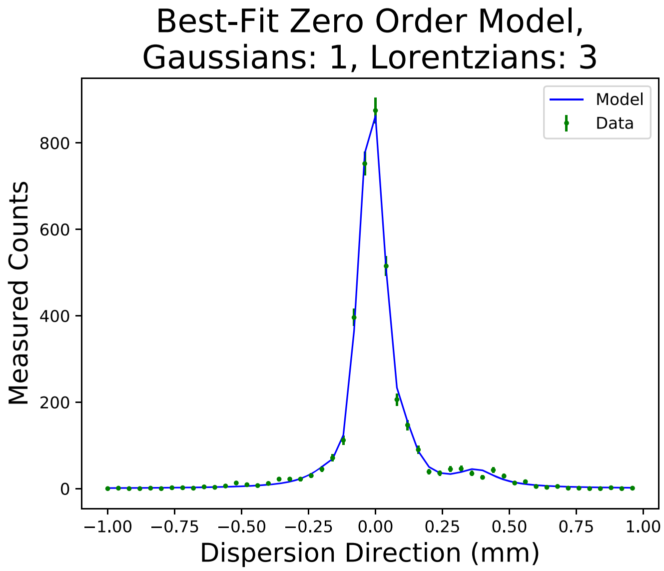

Figure 11. Best-fit zeroth-order model based on the BIC merit function. Data points with Poisson errors are shown in green, with the model shown as a blue line.

proportional to the product of the individual order likelihoods given a shared parameter set θ as given in Section 3.4.

Furthermore, given the dependence on the LSF model $F(x, n, \theta)$ on the zeroth-order model $F(x, n = 0, \theta)$, the posterior probability distribution of the fit parameters is informed by the fit to the zeroth-order data described in Section 3.5. We therefore employ the posterior probability distribution of the best-fit zeroth-order model fit described in Section 3.5 as a prior $P(\theta)$ in the ensemble LSF fitting. This formulation does not constrain the MCMC sampling to the zeroth-order best-fit parameters shown in Figure 11, but instead enables the MCMC chain to sample the full distribution of possible parameters subject to the likelihood that those parameters also describe the zeroth-order data. In essence, this incorporates errors associated with the zeroth-order fit into the ensemble LSF fit.

The resulting fits to the 27th-, 29th-, and 30th-order data are shown in Figure 12, while the distribution of the shared parameter R is shown in Figure 13. Based on this posterior distribution, we estimate $R = 2600$ for this grating and establish a lower bound of $R > 2200$ (0.135%, 3σ equivalent).

4. Discussion

4.1. Achieved Resolution

The best-fit resolution $R = 2600$ of this realized spectrometer system represents a factor of 2–6× improvement over the spectral resolutions of the XMM RGS and the Chandra HETG/LETG. This performance, however, falls short of the Lynx performance requirement of $R > 5000$. The as-measured grating resolution may be limited by (1) a geometric aberration arising from path length differences across the width of the grating, (2) defocus error due to measurements of the diffracted LSFs at a focal plane displaced from the ideal, (3) a displacement of the grating along the optical axis, resulting in a mismatch of the beam's convergence with the fanned ruling of the grating grooves, or (4) period errors in the as-fabricated grating.

The first limitation results from the path length difference over the finite width of the grating for diffracted rays, which

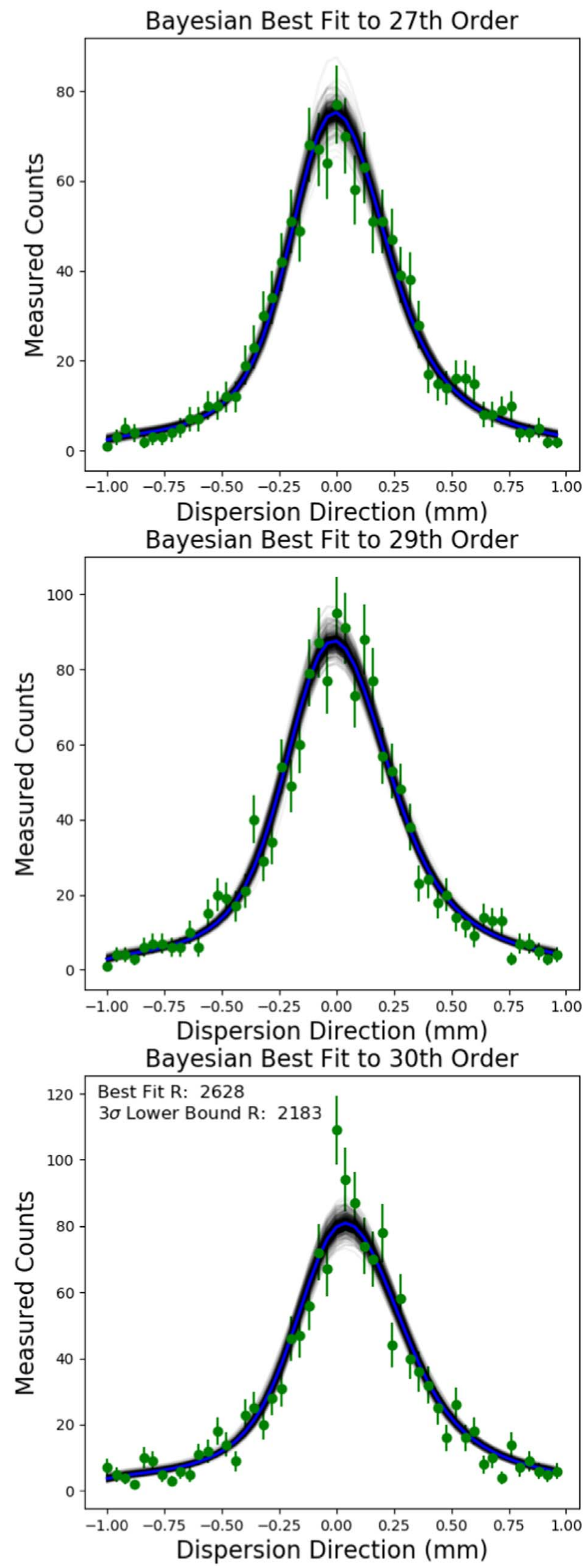

Figure 12. Results of the ensemble fit to the diffracted orders. The measured data are shown in green with Poisson error bars, and the best-fit model as the thick blue line. A total of 500 model realizations (thin, light lines) are drawn randomly from the MCMC chain to demonstrate the range of model fits consistent with the posterior distribution.

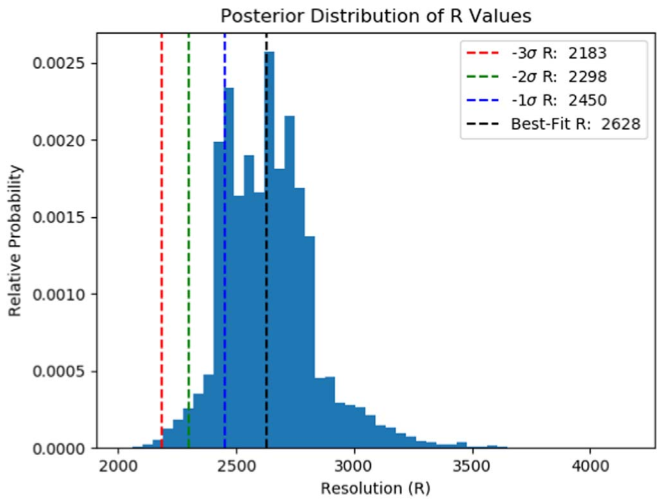

Figure 13. Full distribution of R values sampled by the MCMC chain. The best-fit resolution R and the 3σ lower bound are drawn from this distribution.

travel different distances to reach the focal plane. The result is a purely geometric aberration to the diffracted LSF, rotating the LSF about the chief ray and projecting the radial extent of the optic's PSF onto the dispersion direction. For a subapertured, X-ray optic, the focus quality in the radial direction is worse than the performance in the azimuthal direction Thus, this geometric effect broadens the LSF in the dispersion direction. Furthermore, the magnitude of the broadening is dependent on the functional form of the optic's PSF. The second potential issue, defocus, results from a focal plane displaced from the position of best focus, broadening the measured LSF. Third, a displacement of the grating along the optical axis yields a groove density that changes over the axial length of the grating more or less rapidly than it should to match the convergence of the telescope beam. Finally, period errors in the as-fabricated grating would degrade the achieved resolution, as groove period errors alter the dispersion $\partial\lambda/\partial x$ over the area of the grating.

We assess potential limiting factors in the achieved grating resolution by performing a ray-trace simulation of the spectrometer system as assembled at PANTER using *PyXFocus*.[8] The ray-trace employs a single perfect grating illuminated by an SPO and uses geometric parameters analogous to those presented in Table 1 and distances as reported in Figure 3. Wavelengths for the simulated rays are drawn from the probability distribution function of the Al K$\alpha_{1,2}$ line as parameterized by Table 2. To facilitate direct comparison to the measured LSFs, we simulate only as many photons as detected during each PANTER measurement. The ray-traced photons are binned to 40 μm to form an image, in keeping with the measured photons. FWHM values are calculated from these simulated images in the same manner as the measured CCD images. Errors in the simulated FWHM values are estimated by repeating the ray-trace simulation 100 times and computed using the standard deviation of the FWHM values.

We incorporate Gaussian slope errors into our ray-trace model of the XOU to mimic the overall performance of the telescope. While we do not match the functional form of the SPO PSF, comparison between the measured SPO focus and that produced via the ray-trace simulation (Figure 14) shows good qualitative agreement. Moreover, the width of the measured SPO PSF in the dispersion direction, $\mathrm{FWHM}_{\mathrm{SPO}}^{\mathrm{meas}} = 106 \pm 2\ \mu$m, and the width of the simulated SPO PSF, $\mathrm{FWHM}_{\mathrm{SPO}}^{\mathrm{sim}} = 107 \pm 2\ \mu$m, agree to within error.

We next employ the same ray-trace model to simulate the diffracted 30th-order LSF. Figure 15 compares the measured and simulated diffracted LSFs, as well as their projections along the dispersion direction. We find that our ray-trace simulation agrees with the measured 30th-order LSF to within their estimated errors ($\mathrm{FWHM}_{30}^{\mathrm{meas}} = 394 \pm 11\ \mu$m vs. $\mathrm{FWHM}_{30}^{\mathrm{sim}} = 411 \pm 38\ \mu$m). The ray-trace merely simulates the diffraction geometry and does not include defocus, a mismatched ruling of the grating grooves, or period error. Based on the agreement between the ray-trace simulation and the measured diffracted LSFs, we find that the geometric aberration fully accounts for the calculated grating resolution in this test configuration.

This has implications for the design of grating spectrometers employing reflection gratings in a conical mounting. Previous spectrometer design efforts idealize the PSF produced by the telescope feeding the grating array. However, as demonstrated with these measurements and the supporting ray-trace study, an accurate parameterization is crucial, since the instrument resolution may become limited by the performance of the telescope in the radial direction owing to this geometric aberration. This stands in contrast to design efforts that assume that resolution is dependent on the performance of the optic in the subapertured dimension alone. An accurate representation of the PSF to be employed is needed to accurately assess the achievable resolution for an X-ray reflection grating spectrometer.

While the remaining potential factors that could limit the measured resolution are unable to be constrained by these data given the dominance of the geometric error term, we find that they are unlikely to be major contributors given the magnitude of the alignment or fabrication errors required to achieve $R = 2600$. To estimate the degree of defocus or grating misalignment along the optical axis needed, we assume $R \sim x/\Delta x$, where x is the distance dispersed from zeroth order and Δx is the growth of the LSF in the dispersion direction resulting from misalignment. Based on the rate of convergence of the SPO beam in the dispersion direction, we find that the focal plane would need to be displaced by approximately 100 mm to yield a Δx comparable to the achieved resolution. In contrast, we estimate that the position of best focus of the diffracted orders is known to ± 20 mm based on focus scans of the detector along the optical axis during the diffracted order measurement. Turning to the mismatch of beam convergence to grating groove convergence, we employ the constructed ray-trace of the PANTER system. We simulate a perfect optic and grating but intentionally misalign the grating by translating it along the chief ray of the telescope beam within the ray-trace by an amount Δz. The rays are then diffracted and proceed to the as-measured focal plane, and the resulting Δx is measured by taking the FWHM of the resulting LSF. For a single grating, a translation Δz of approximately 2 m is needed before yielding a Δx large enough to yield $R = 2600$. As this is two orders of magnitude larger than the measurement error associated with our measurement of the distance between the groove hub and the center of the grating (see Figure 3), we dismiss this misalignment as a significant limiting factor in the grating resolution reported.

[8] https://github.com/rallured/PyXFocus

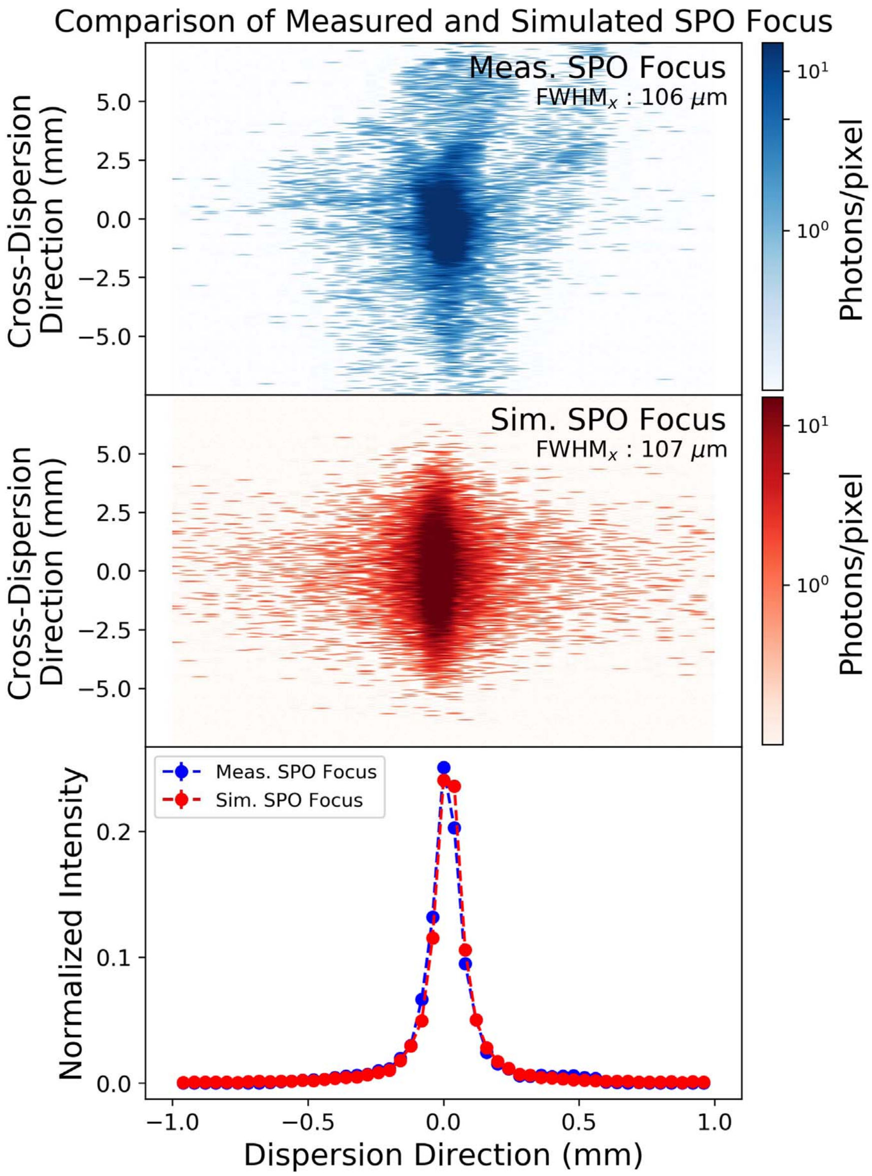

Figure 14. Measurements of the measured SPO focus (top), the SPO focus simulated via ray-trace (middle), and the dispersion profiles of each (bottom).

Finally, we assess the possibility of groove period error by computing the variation required to yield $R = 2600$. As $\partial\lambda/\partial x$ is linearly proportional to d^{-1}, the period error required to yield a resolution R can be estimated as $R \sim d/\Delta d$. With a nominal period of $d = 400$ nm and $R = 2600$, $\Delta d = 0.15$ nm. While we do not have direct measurements of the groove period error of the grating tested, gratings with similar periods produced using EBL for X-ray synchrotron applications have been measured to have smaller Δd by two orders of magnitude (Voronov et al. 2017). Thus, we posit that groove period error is not the dominant limiting factor in the achieved resolution. However, improving the constraints on groove period error would place a definite bound on the achievable resolution performance using EBL-written gratings. The patterning fidelity of EBL-written gratings can be assessed directly by interferometric measurements. By placing a parallel-groove grating measured in the Littrow (back-diffracting) condition, the groove placement accuracy over the entire grating surface can be measured (Hutley 1982). This has the distinct advantage of being performed at optical wavelengths without the overhead of X-ray testing. A dedicated study of the patterning accuracy achieved with the EBL process used for these astronomical reflection gratings would constrain the resolutions achievable with these gratings and be an important input into grating spectroscopy missions.

4.2. Implications for Soft X-Ray Spectroscopy Missions

The grating spectrometer system tested in this work meets the threshold resolution requirement for the notional mission outlined by B15. The figure of merit for the detection of a weak absorption-line feature scales as $\sqrt{\mathrm{EA} \times R}$. Thus, adopting the conservative 3σ lower bound on R while realizing the same figure of merit as the threshold mission outlined by B15 requires an instrument EA of 300 cm^2 at 0.5 keV.

We estimate the EA of an X-ray telescope and detector system that would be required to meet this EA threshold and enable this notional mission. We assume diffraction efficiencies consistent with those reported by Miles et al. (2018) ($\geqslant$60%) for X-ray diffraction gratings operated in an echelle mounting

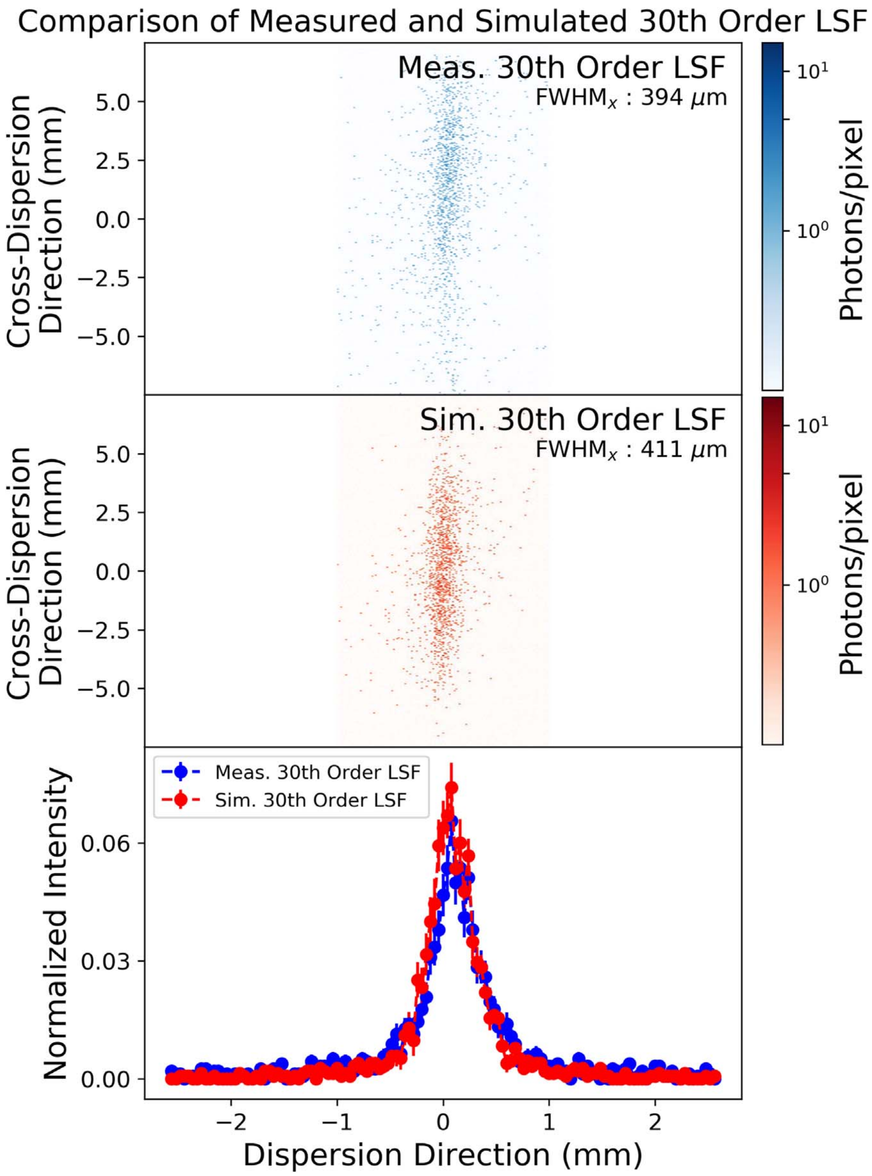

Figure 15. Measurements of the measured 30th-order LSF (top), the 30th-order LSF simulated via ray-trace (middle), and the dispersion profiles of each (bottom).

similar to the present work. We also assume 40% losses from vignetting due to the grating support structure and gaps in grating coverage of the aperture. Based on these assumptions, an X-ray telescope and detector system with $\sim$850 cm^2 of EA at 0.5 keV would yield performance in keeping with the mission outlined by B15. This is approximately 60% of the EA of the XMM-Newton telescopes as measured at the beginning of the mission (Gondoin et al. 2000) or 75% of the EA of the MIDEX Arcus telescope and CCD system (Smith et al. 2019). Thus, a soft X-ray grating spectrometer that uses X-ray reflection gratings operated in an echelle mounting and meets the performance requirements as outlined in B15 may be feasible in a NASA format smaller than a dedicated flagship, such as a Probe or Explorer.

5. Conclusions and Future Work

In the present work, we have measured the LSFs produced by a large-format X-ray reflection grating designed for use in a future soft X-ray spectrograph. This grating was fabricated using EBL and was patterned to match the rate of convergence for a grazing incidence X-ray telescope. Our measurements were conducted at the PANTER X-ray Test Facility and used single SPO XOU to form a single grating spectrometer. This optical system permits the assessment of the spectral resolution intrinsic to the grating. Our measurements were conducted with the grating in an echelle-like mounting, permitting access to high orders dispersed far from zeroth order.

We find evidence for broadening of the zeroth-order LSF on the order of $\sim 1''$ due to grating figure. This is supported by optical figure measurements of the grating in the same mounting as employed during X-ray testing. We model the zeroth-order LSF, as well as the diffracted 27th-, 29th-, and 30th-order Al K$\alpha_{1,2}$ LSFs, to assess the spectral resolution of the grating. A Bayesian MCMC technique is used to explore the range of spectral resolutions that are consistent with the measured grating data.

We find a best-fit resolution of $R = 2600$, with a 3σ lower bound of $R > 2200$. This resolution does not meet the Lynx grating spectrometer requirement of $R > 5000$. We posit that the spectral resolution of these gratings as tested is limited by the geometry of the test configuration, as a ray-trace study of the PANTER measurement configuration yields the observed LSF broadening without defocus, misalignment, or groove period error modeling. The designs of future X-ray reflection grating spectrometers will need to assess this geometric term with detailed ray-trace simulations of a realistic optic PSF and in the context of a holistic error budget. However, X-ray reflection gratings in echelle-like mountings at the currently assessed spectral resolution of $R > 2000$ enable smaller-scale missions.

Given the success of EBL in fabricating high-resolution gratings for synchrotron applications, adapting this technique for the fabrication of X-ray gratings for astronomy is promising. A dedicated study of the groove period error for gratings made using this EBL fabrication process can be performed using an optical interferometer by aligning the grating such that the incidence and diffraction angles are identical. These measurements would constrain the groove period error of gratings written with the EBL process employed here and therefore offer improved insight into the potential performance limitations of X-ray reflection gratings.

While measurements of the groove period error provide an upper bound on the resolution of X-ray reflection gratings, additional X-ray measurements are needed to empirically quantify the impact of other error terms that degrade spectral resolution in an astronomical instrument. Assessing the magnitude of these error terms in diffracted orders accurately requires minimizing the contribution of the zeroth-order LSF to these measurements. Hence, testing gratings with better optical figure in conjunction with telescopes that have improved angular resolution would be highly desirable. Moreover, such a system would be more representative of a future high spectral resolution grating spectroscopy mission such as Lynx.

Fabrication studies to produce a blazed conical reflection grating are ongoing. Such a grating would enable deeper measurements during the limited windows for X-ray testing, improving the statistical power of the analysis performed here. Furthermore, a blazed grating would improve measurement throughput and hence would enable testing in conical geometries in which γ and β are varied. These measurements would serve as an empirical check on predicted geometric aberrations and are important feedback to the X-ray spectrometer design process. Finally, and most crucially, blazed conical reflection gratings would substantially increase spectrometer throughput at high orders for a flight instrument. This would enable missions capable of detecting hot baryonic material in the halos of galaxies and clusters in absorption and hence could address outstanding problems in simulations of large-scale structure and feedback.

We acknowledge helpful conversations with S. Spangler about the merits of a Bayesian approach. We thank the anonymous referee for the constructive feedback on the manuscript. This work was supported by NASA grants NNX17AD19G, NNX17AC88G, and NNX15AC42G. This work makes use of *PyXFocus*, an open-source Python-based ray-tracing package.

ORCID iDs

Casey T. DeRoo https://orcid.org/0000-0002-9184-4561
Randall L. McEntaffer https://orcid.org/0000-0002-3719-8212
Benjamin D. Donovan https://orcid.org/0000-0002-0253-7851
Fabien Grisé https://orcid.org/0000-0002-3603-9789

References

Barriére, N. M., Vacanti, G., Verhoeckx, S., et al. 2019, Proc. SPIE, 11119, 111190J
Bavdaz, M., Wille, E., Ayre, M., et al. 2019, Proc. SPIE, 11119, 111190D
Bearden, J. A., & Burr, A. F. 1967, RvMP, 39, 78
Bradshaw, M., Burwitz, V., Hartner, G., et al. 2019, Proc. SPIE, 11119, 1111916
Bregman, J. N. 2007, ARA&A, 45, 221
Bregman, J. N., Alves, G. C., Miller, M. J., & Hodges-Kluck, E. 2015, JATIS, 1, 045003
Brinkman, B., Gunsing, T., Kaastra, J., et al. 2000, Proc. SPIE, 4012, 81
Burwitz, V., Bavdaz, M., Wille, E., et al. 2019, Proc. SPIE, 11180, 1118024
Canizares, C. R., Davis, J. E., Dewey, D., et al. 2005, PASP, 117, 1144
Cash, W. 1979, ApJ, 228, 939
Cash, W. 1982, ApOpt, 21, 710
Cen, R., & Ostriker, J. 2006, ApJ, 650, 560
Collon, M. J., Vacanti, G., Barriére, N. M., et al. 2019, Proc. SPIE, 11119, 111190L
Danforth, C. W., & Shull, J. M. 2008, ApJ, 679, 194
de Graaff, A., Cai, Y.-C., Heymans, C., & Peacock, J. A. 2019, A&A, 624, A48
den Herder, J. W., Brinkman, A. C., Kahn, S. M., et al. 2001, A&A, 365, L7
Foreman-Mackey, D., Hogg, D. W., Lang, D., & Goodman, J. 2013, PASP, 125, 306
Gaskin, J. A., Swartz, D., Vikhlinin, A. A., et al. 2019, JATIS, 5, 021001
Gondoin, P., Aschenbach, B., Erd, C., et al. 2000, Proc. SPIE, 4140
Goodman, J., & Weare, J. 2010, Commun. Appl. Math. Comput., 5, 65
Heilmann, R. K., Kolodziejczak, J., Bruccoleri, A. R., Gaskin, J. A., & Schattenburg, M. L. 2019, ApOpt, 58, 1223
Hutley, M. 1982, Diffraction Gratings (Cambridge, MA: Academic Press)
Keek, L., Babić, L., Barriére, N. M., et al. 2019, Proc. SPIE, 11119, 111190H
Kovács, O., Bogdán, A., Smith, R., Kraft, R. P., & Forman, W. R. 2019, ApJ, 872, 83
Landgraf, B., Collon, M., Vacanti, G., et al. 2019, Proc. SPIE, 11119, doi:10.1117/12.2530941
Lehner, N., Savage, B. D., Richter, P., et al. 2007, ApJ, 658, 680
Manfrinato, V. R., Zhang, L., Su, D., et al. 2013, NanoL, 14, 1555
McEntaffer, R., DeRoo, C., Schultz, T., et al. 2013, ExA, 36, 389
McEntaffer, R. L. 2019, JATIS, 5, 021002
Meidinger, N., Andritschke, R., Ebermayer, S., et al. 2009, Proc. SPIE, 7435
Miles, D., McCoy, J. A., McEntaffer, R. L., et al. 2018, ApJ, 869, 95
Miles, D. M., Hull, S. V., Schultz, T. B., et al. 2019, JATIS, 5, 044006
Nelder, J. A., & Mead, R. 1965, CompJ, 7
Newville, M., Otten, R., Nelson, A., et al. 2019, lmfit/lmfit-py v 0.9.14, Zenodo, doi:10.5281/zenodo.3381550
Oakley, P., McEntaffer, R., & Cash, W. 2013, ApJ, 766, 51
Predehl, P., Andritschke, R., Babshkin, V., et al. 2016, Proc. SPIE, 9905
Raftery, A. E., & Lewis, S. M. 1992, in Bayesian Statistics 4, ed. J. M. Bernardo et al. (London: Oxford Univ. Press), 763
Saha, T. T., Chan, K.-W., Mazzarella, J. R., et al. 2018, Proc. SPIE, 10699, 1069952
Schwarz, G. 1978, AnSta, 6, 461
Shull, J. M., Smith, B. D., & Danforth, C. W. 2012, ApJ, 759, 23
Smith, R. K., Abraham, M., Baird, G., et al. 2019, Proc. SPIE, 11118, 111180W
Tanimura, H., Hinshaw, G., McCarthy, I. G., et al. 2019, MNRAS, 483, 223
Vacanti, G., Barriére, N. M., Collon, M. J., et al. 2019, Proc. SPIE, 11119, 111190I
Voronov, D. L., Gullikson, E. M., & Padmore, H. A. 2017, OExpr, 25, 23334